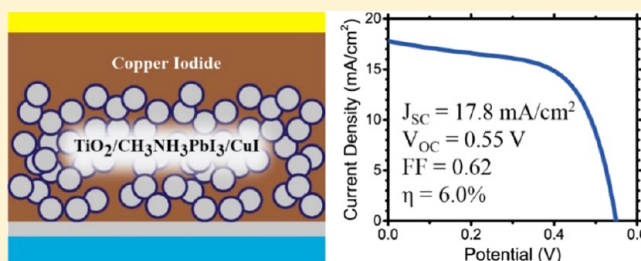


# An Inorganic Hole Conductor for Organo-Lead Halide Perovskite Solar Cells. Improved Hole Conductivity with Copper Iodide

Jeffrey A. Christians,<sup>†,§</sup> Raymond C. M. Fung,<sup>†,#</sup> and Prashant V. Kamat<sup>\*,†,§,‡</sup><sup>†</sup>Radiation Laboratory, University of Notre Dame, Notre Dame, Indiana 46556, United States<sup>§</sup>Department of Chemical and Biomolecular Engineering, University of Notre Dame, Notre Dame, Indiana 46556, United States<sup>‡</sup>Department of Chemistry and Biochemistry, University of Notre Dame, Notre Dame, Indiana 46556, United States

## S Supporting Information

**ABSTRACT:** Organo-lead halide perovskite solar cells have emerged as one of the most promising candidates for the next generation of solar cells. To date, these perovskite thin film solar cells have exclusively employed organic hole conducting polymers which are often expensive and have low hole mobility. In a quest to explore new inorganic hole conducting materials for these perovskite-based thin film photovoltaics, we have identified copper iodide as a possible alternative. Using copper iodide, we have succeeded in achieving a promising power conversion efficiency of 6.0% with excellent photo-current stability. The open-circuit voltage, compared to the best spiro-OMeTAD devices, remains low and is attributed to higher recombination in CuI devices as determined by impedance spectroscopy. However, impedance spectroscopy revealed that CuI exhibits 2 orders of magnitude higher electrical conductivity than spiro-OMeTAD which allows for significantly higher fill factors. Reducing the recombination in these devices could render CuI as a cost-effective competitor to spiro-OMeTAD in perovskite solar cells.



## INTRODUCTION

With the continued rise in global energy demand, there is a growing need to transition from fossil fuels to renewable energy sources to promote a cleaner atmosphere and reduce global warming.<sup>1</sup> The Sun delivers more energy to Earth's surface in 1 h than humanity currently uses in one year. Therefore, harvesting a small fraction of incident solar irradiation could meet our growing energy demand. Realizing the full potential of this vast energy source requires a new generation of photovoltaics that are both efficient and cost-effective.<sup>2</sup> For this reason, solid-state heterojunction solar cells have been the subject of ongoing investigation.<sup>3–5</sup> Additionally, such thin film solar cells have a lower carbon footprint and shorter energy payback period in comparison to wafer-based technologies which contribute to making these devices more environmentally friendly.<sup>6,7</sup>

Solar cells employing methylammonium lead iodide (CH<sub>3</sub>NH<sub>3</sub>PbI<sub>3</sub>) perovskite absorber materials on mesoscopic TiO<sub>2</sub> and Al<sub>2</sub>O<sub>3</sub> substrates have shown very promising efficiencies over 10%.<sup>3,4,8–11</sup> These perovskite solar cells have typically employed a wide variety of organic polymer hole conductors.<sup>8–10,12,13</sup> Most notable of these hole-conducting polymers is spiro-OMeTAD (2,2',7,7'-tetrakis(*N,N*-di-*p*-methoxyphenylamine) 9,9'-spirobifluorene). Using spiro-OMeTAD as hole conductor, Burschka et al. recently constructed a TiO<sub>2</sub>/CH<sub>3</sub>NH<sub>3</sub>PbI<sub>3</sub> solar cell demonstrating 15.0% efficiency,<sup>8</sup> and Liu et al. reported a planar TiO<sub>2</sub>/CH<sub>3</sub>NH<sub>3</sub>PbI<sub>3–x</sub>Cl<sub>x</sub> solar cell with a record efficiency of 15.4%.<sup>14</sup>

The high efficiency obtained with these perovskite sensitizers demonstrates their potential for implementation as commercial solar cells.<sup>3,11</sup> However, the use of organic hole conductors may represent a potential hurdle to the future commercialization of this type of solar cell because of their relatively high cost. For example, the current commercial price of high purity spiro-OMeTAD is over ten times that of gold and platinum. While increased demand would undoubtedly lower this cost dramatically in any large scale commercial endeavor, it is likely to remain expensive due to the synthetic methods and high purity needed for photovoltaic applications.<sup>17</sup> On the other hand, inorganic copper-based p-type semiconductors, such as CuSCN and CuI, offer potential hole conductors for a much lower cost. Also, these copper-based hole conductors have shown promise for use in dye-sensitized and quantum dot-sensitized solar cells because they are solution-processable, wide-band-gap semiconductors with high conductivity.<sup>18–23</sup> Furthermore, there have been numerous reports of inorganic hole conductors used in sensitized solar cells which outperform comparable spiro-OMeTAD solar cells.<sup>24–26</sup> For this reason, development of alternative hole conductors to spiro-OMeTAD is a promising avenue to further improve the performance of perovskite solar cells, as spiro-OMeTAD likely does not represent the ideal hole-conducting material for this system. In this study, we present a CH<sub>3</sub>NH<sub>3</sub>PbI<sub>3</sub> perovskite-sensitized

Received: October 28, 2013

Published: December 18, 2013

solar cell utilizing CuI as the hole conductor, demonstrating an inexpensive, stable, solution-processable inorganic hole conductor. CuI was selected on the basis of its suitable valence band position (Figure 1),<sup>15,16</sup> high p-type conductivity, and the compatibility of the solution deposition method with the organo-lead halide perovskite absorber.

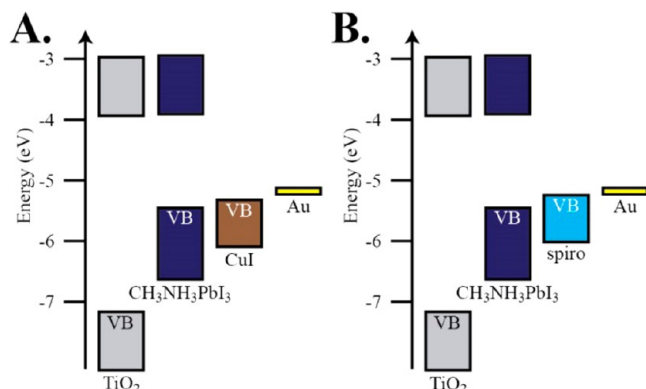


**Figure 1.** Band energy diagram of  $\text{TiO}_2/\text{CH}_3\text{NH}_3\text{PbI}_3$  solar cell employing (A) CuI and (B) spiro-OMeTAD hole conductors.<sup>15,16</sup>

## EXPERIMENTAL SECTION

**Materials.** 2,2',7,7'-Tetrakis(*N,N*-di-*p*-methoxyphenylamine)-9,9-spirobifluorene (spiro-OMeTAD, Luminescence Technology Corp.), 4-*tert*-butylpyridine (Sigma Aldrich, 99%), bis(trifluoromethane)sulfonamide lithium salt (Sigma Aldrich, 97%), chlorobenzene (Alfa Aesar, 99.5%), copper iodide (Sigma Aldrich, 98%), di-*n*-propyl sulfide ( $\text{C}_6\text{H}_{14}\text{S}$ , Alfa Aesar, 98%), hydroiodic acid (Alfa Aesar, 55–58 wt %),  $\gamma$ -butyrolactone (Sigma Aldrich, 99+%), lead iodide (Arcos Organics, 99%), methylamine (Sigma Aldrich, 40 wt % in  $\text{H}_2\text{O}$ ), titanium diisopropoxide bis(acetylacetonate) ( $[(\text{CH}_3)_2\text{CHO}]_2\text{Ti}(\text{C}_6\text{H}_7\text{O}_2)_2$ , Sigma Aldrich, 75 wt % in 2-propanol), and zinc powder (median 6–9  $\mu\text{m}$ , Alfa Aesar, 97.5%) were used without further purification.

**Synthesis of Methylammonium Iodide.** Methylammonium lead iodide was synthesized by the dropwise addition of hydroiodic acid (aqueous, 57 wt %) to a solution of methylamine (aqueous, 40 wt %) in an ice bath. The cold solution was stirred for 2 h, and the solvent was evaporated using a rotary evaporator. The crystals were washed using diethyl ether three times and dried. The resulting white solid was used without further purification.

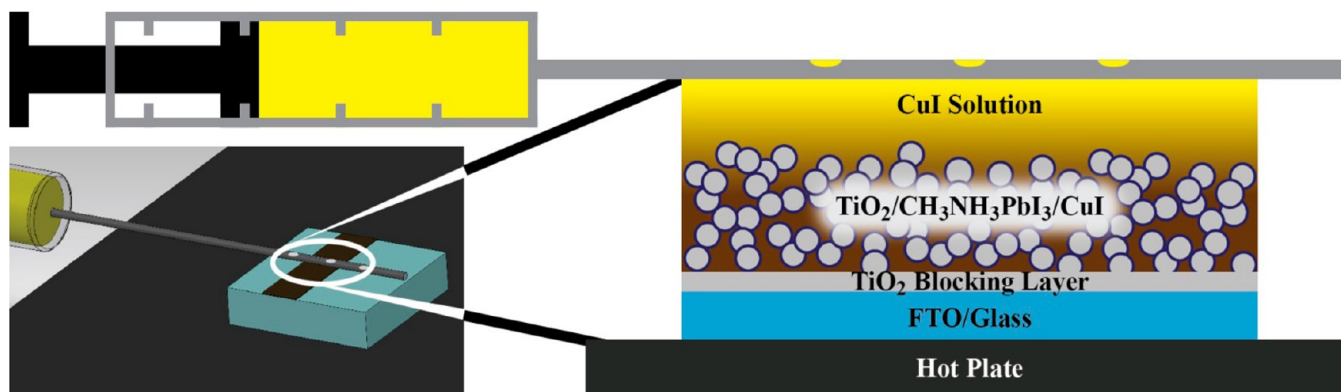
**Solar Cell Fabrication.** Solar cells were fabricated in a dry environment. Fluorine-doped tin oxide (FTO) glass (Pilkington Glass, TEC-7, 2 mm thickness) was masked, and the exposed area was coated

in Zn powder. The FTO layer was then etched away by dripping  $\sim 2\text{ M}$  HCl over the Zn. The etched FTO glass slides were then rinsed with DI  $\text{H}_2\text{O}$  and cleaned for 15 min using a detergent solution in an ultrasonic bath. The glass was rinsed with water and then ethanol, dried with air, and heated at  $500^\circ\text{C}$  for 5 min to remove any organics. A ca. 100 nm compact  $\text{TiO}_2$  blocking layer was deposited on the FTO by spray pyrolysis of 0.20 M titanium diisopropoxide bis(acetylacetonate) (TAA) in ethanol.<sup>27</sup> The films were then annealed at  $500^\circ\text{C}$  for 30 min. The mesoporous  $\text{TiO}_2$  layer was spin coated from a  $\text{TiO}_2$  paste (Dyesol 18 NR-T paste 2.5:1 dilution by weight in anhydrous ethanol) at 2000 rpm for 30 s. The films were dried at  $80^\circ\text{C}$  for 30 min and annealed at  $500^\circ\text{C}$  for 1 h. The  $\text{CH}_3\text{NH}_3\text{PbI}_3$  precursor solution was prepared by dissolving equimolar amounts of  $\text{CH}_3\text{NH}_3\text{I}$  and  $\text{PbI}_2$  in anhydrous  $\gamma$ -butyrolactone (40% by weight) at  $70^\circ\text{C}$ . This solution was dripped on top of the  $\text{TiO}_2$  film, and the film was soaked for 1 min and then spun at 2000 rpm for 30 s. The film was placed on a hot plate at  $80^\circ\text{C}$  for 45 min to form crystalline  $\text{CH}_3\text{NH}_3\text{PbI}_3$ . For spiro-OMeTAD films, the spiro-OMeTAD hole conductor was applied by spin coating a solution of 68 mM spiro-OMeTAD, 55 mM *tert*-butylpyridine, and 9 mM lithium bis-(trifluoromethylsulfonyl)imide salt in chlorobenzene at 2000 rpm for 45 s. The CuI hole conductor was deposited as described below. Following hole conductor deposition, the solar cells were stored in a desiccator overnight. Finally, the solar cells were completed by depositing a gold contact (100 nm) by metal evaporation. The completed solar cells were then scribed (typical area of  $\sim 0.15\text{ cm}^2$ ) to separate the solar cell active area from the surrounding material before testing. The efficiency of CuI solar cells typically improved, mainly because of an increased open-circuit voltage and short-circuit current, upon storage in dry air in the dark for several days to two weeks following completion.

For absorbance measurements, mesoporous  $\text{Al}_2\text{O}_3$  films were prepared by spin coating in a manner similar to that for the  $\text{TiO}_2$  films. A 20 wt % solution of  $\text{CH}_3\text{NH}_3\text{I}$  and  $\text{PbI}_2$  was cast onto the  $\text{Al}_2\text{O}_3$  films and annealed to form crystalline  $\text{CH}_3\text{NH}_3\text{PbI}_3$ .

**Copper Iodide Deposition.** Copper iodide was dissolved in 1:39 di-*n*-propyl sulfide to chlorobenzene, respectively, to form a 0.1 M CuI solution by stirring overnight. This solution was used to deposit CuI onto the sensitized  $\text{TiO}_2$  film using an apparatus similar to that reported by O'Regan et al. for CuSCN deposition,<sup>28</sup> as shown in Scheme 1. Holes were drilled (0.3 mm, spaced  $\sim 3\text{ mm}$  apart) into the side of a needle (0.7 mm diameter). The FTO substrate ( $2\text{ cm} \times 1.5\text{ cm}$ ) was placed on a hot plate at  $80^\circ\text{C}$  with the deposition needle aligned parallel approximately 0.5 mm above the surface. CuI solution was pumped at a constant rate of  $25\ \mu\text{L min}^{-1}$  using a syringe pump until a small bead of solution formed between the bottom of the needle and the surface of the solar cell across the entire width of the FTO. The needle was then moved back and forth above the surface of the electrode at a rate of  $1\text{ mm s}^{-1}$  while the CuI solution slowly infiltrated the  $\text{TiO}_2$  pores. This technique allowed for thin films of CuI

**Scheme 1.** Automated Drop-Casting Apparatus Used in Our Lab for the Solution Deposition of CuI onto Mesoporous  $\text{TiO}_2/\text{CH}_3\text{NH}_3\text{PbI}_3$  Films





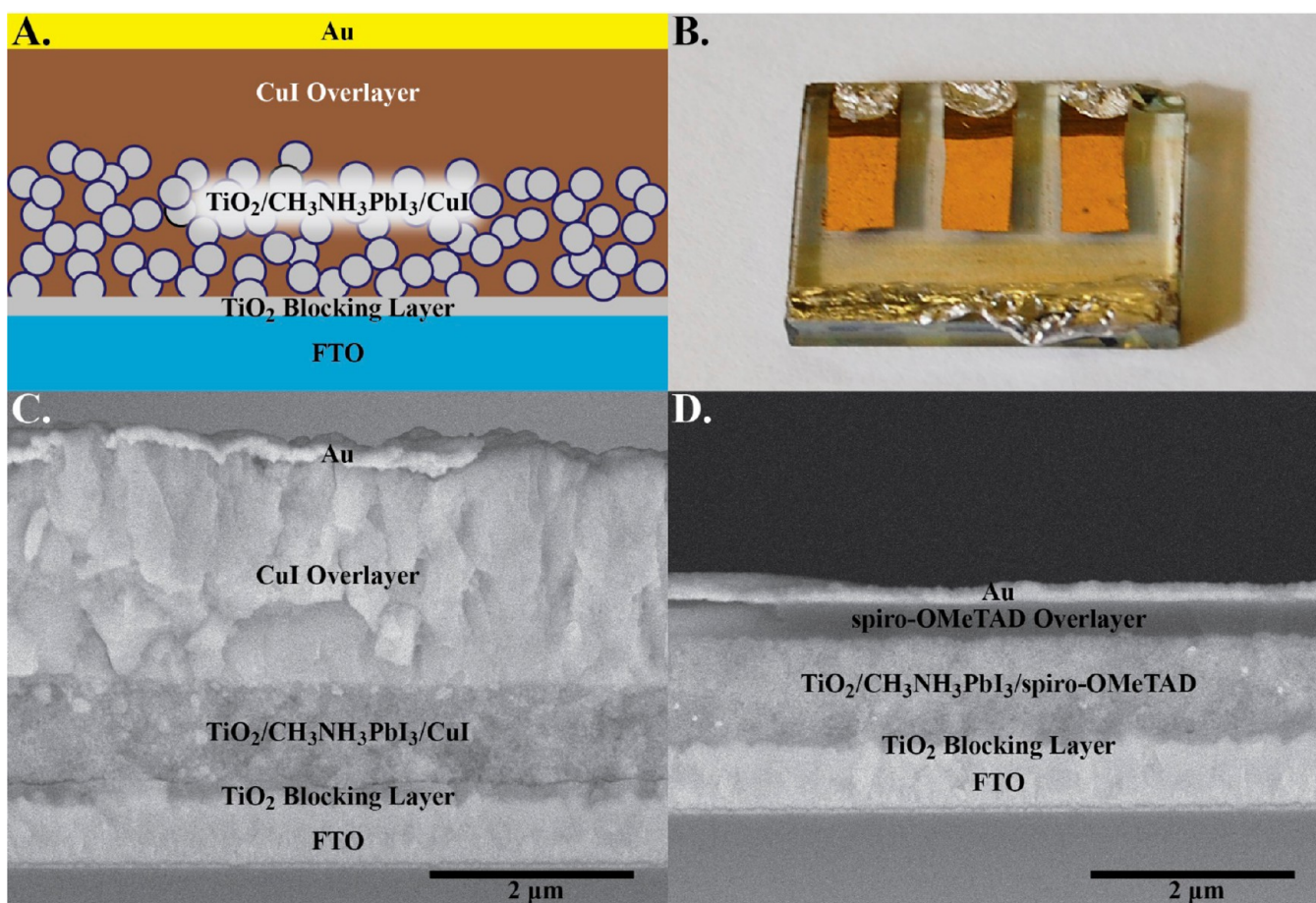


**Figure 2.** (A) Cross section schematic of  $\text{TiO}_2/\text{CH}_3\text{NH}_3\text{PbI}_3/\text{CuI}$  solar cell and (B) image of the complete device. SEM cross section images of solar cells employing (C) CuI and (D) spiro-OMeTAD hole conductors.

to be spread over the solar cell active area and dried before the next film was applied. In this way, CuI was allowed to build up in the mesoporous  $\text{TiO}_2$  network and form a 1.5–2.0  $\mu\text{m}$  overlayer. After deposition, the excess CuI was scribed off of the electrode areas before the Au contact deposition.

**Impedance Spectroscopy.** Impedance spectroscopic measurements were performed with a 10 mV rms amplitude over the frequency range of 1 Hz to 300 kHz under 100  $\text{mW}/\text{cm}^2$  AM 1.5G simulated solar irradiation. Gamry E-Chem Analyst software was used to model the Nyquist plots obtained from the impedance measurements.

**Characterization.** UV–visible absorption measurements were conducted using a Varian Cary 50 Bio spectrophotometer. Photoelectrochemical measurements were carried out using a Princeton Applied Research 2273 (PARstat) potentiostat. A 300 W Xe lamp with an AM 1.5 filter was used to illuminate the solar cells at 100  $\text{mW}/\text{cm}^2$ . Incident photon to carrier efficiencies (or EQE) were measured using a Newport Oriel QE/IPCE measurement kit with a silicon photodiode detector. Film cross sections were obtained using an FEI Magellan-400 field emission scanning electron microscope (FESEM).

## RESULTS AND DISCUSSION

**Fabrication and Characterization of Solar Cells.**  $\text{TiO}_2/\text{CH}_3\text{NH}_3\text{PbI}_3$  solar cells utilizing either CuI or spiro-OMeTAD hole conductors were constructed by similar methods as discussed previously in the literature.<sup>29</sup> Briefly, a  $\sim 100$  nm compact  $\text{TiO}_2$  blocking layer was deposited on the FTO by spray pyrolysis,<sup>27</sup> and the 600–800 nm thick  $\text{TiO}_2$  active layer was applied by spin-coating. The  $\text{TiO}_2$  films were dried for 30 min at 80  $^\circ\text{C}$  and sintered at 500  $^\circ\text{C}$  for 1 h. The perovskite was

deposited by spin-coating a 40 wt % equimolar solution of  $\text{CH}_3\text{NH}_3\text{I}$  and  $\text{PbI}_2$  in  $\gamma$ -butyrolactone. The films were then annealed at 80  $^\circ\text{C}$  for 45 min to allow the  $\text{CH}_3\text{NH}_3\text{PbI}_3$  to crystallize.

CuI solar cells were constructed by an automated drop-casting technique pictured in Scheme 1, similar to previously reported methods for CuSCN deposition,<sup>20,21,28</sup> from a 1:39 di-*n*-propyl sulfide–chlorobenzene solution. For this deposition, a syringe needle with holes drilled along the top was placed above the  $\text{TiO}_2/\text{CH}_3\text{NH}_3\text{PbI}_3$  film, which was maintained at 80  $^\circ\text{C}$ , and a bead of CuI solution was moved back and forth across the substrate using an automated mechanical motor. In this way the CuI was deposited over the entire solar cell, filling the porous  $\text{TiO}_2/\text{CH}_3\text{NH}_3\text{PbI}_3$  network and creating a 1.5–2.0  $\mu\text{m}$  CuI overlayer (Figure 2C). Spiro-OMeTAD solar cells were constructed by spin-casting from chlorobenzene onto the  $\text{TiO}_2/\text{CH}_3\text{NH}_3\text{PbI}_3$  film to provide pore filling of mesoporous network and a 200–400 nm spiro-OMeTAD overlayer (Figure 2D). Excess CuI (or spiro-OMeTAD) was scribed off, and a gold contact (100 nm) was deposited using metal evaporation to form the counter electrode. The cell active area was then scribed to separate the measured solar cell area from the surrounding deposit. This was essential for CuI solar cells to prevent artifacts from lateral current flow, as shown in Figure SI-1, Supporting Information.

Upon deposition of CuI into the perovskite film, it is possible that the Cu in the hole conductor reacts with the  $\text{CH}_3\text{NH}_3\text{PbI}_3$ , causing a Cu/Pb exchange or another reaction. If this were to

take place, we would expect to see a shift in the absorbance peaks of the perovskite sensitizer. Therefore, UV–visible absorbance spectra of  $\text{Al}_2\text{O}_3/\text{CH}_3\text{NH}_3\text{PbI}_3$  films were recorded before and after CuI deposition, as shown in Figure SI-2, Supporting Information. The absence of any significant peak shift following CuI deposition indicates that any Cu/Pb exchange or other reaction between the perovskite and the CuI, if it occurs at all, is likely to be small.

**Photoelectrochemical Performance.** Photoelectrochemical performance of these devices was tested under 100  $\text{mW}/\text{cm}^2$  AM 1.5G simulated solar irradiation. CuI solar cells required storage for days to weeks to reach their maximum efficiency. Storage resulted primarily in increased  $V_{\text{OC}}$ , and  $J_{\text{SC}}$ , the fill factor, generally did not change significantly. The  $J$ – $V$  characteristics of the champion CuI and spiro-OMeTAD solar cells are shown in Figure 3. The photoelectrochemical

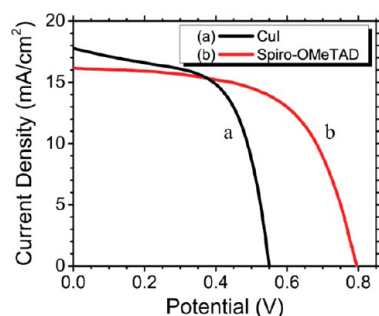


**Figure 3.**  $J$ – $V$  characteristics of champion  $\text{TiO}_2/\text{CH}_3\text{NH}_3\text{PbI}_3$  solar cells employing CuI (green) and spiro-OMeTAD (blue) hole conductors under 100  $\text{mW}/\text{cm}^2$  AM 1.5G irradiation. Solar cell active areas were scribed to be  $0.13 \pm 0.02 \text{ cm}^2$ .

performance of 36 CuI and 48 spiro-OMeTAD solar cells is summarized in Table 1. Complete analyses of the photovoltaic parameters for all CuI and spiro-OMeTAD solar cells tested are shown in Figure SI-3 and Figure SI-4 in the Supporting Information, respectively. The champion CuI solar cell exhibited power conversion efficiency of 6.0% compared to 7.9% for the champion spiro-OMeTAD device. It should be noted that while the champion spiro-OMeTAD devices fabricated in our lab have efficiency lower than that of the best reported devices,<sup>15</sup> the overall distribution of efficiency was very competitive with other reported  $\text{TiO}_2/\text{CH}_3\text{NH}_3\text{PbI}_3$ /spiro-OMeTAD solar cells, as shown in Figure SI-5, Supporting Information.<sup>9,29</sup>

As seen in the summary of device performance in Table 1, the primary difference in photovoltaic performance of the two hole conductors is the low open-circuit voltage of the CuI solar

cells, nearly 300 mV lower on average than that obtained using spiro-OMeTAD.

The external quantum efficiency (EQE) of the CuI and spiro-OMeTAD solar cells were recorded by monitoring short-circuit current at different incident wavelengths of light (Figure 4A). Both CuI and spiro-OMeTAD solar cells show peak

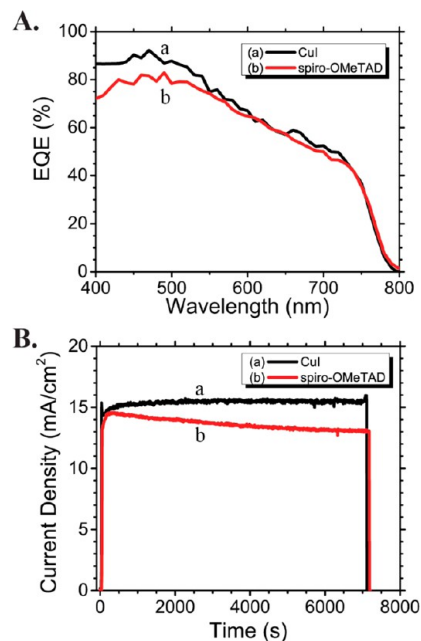


**Figure 4.** (A) IPCE of (a) CuI and (b) spiro-OMeTAD solar cells. (B)  $J_{\text{SC}}$  upon 2 h continuous illumination without encapsulation at 100  $\text{mW}/\text{cm}^2$  AM 1.5 illumination of (a) CuI and (b) spiro-OMeTAD solar cells.

external quantum efficiencies (EQE) over 80%. The solar cells show similar spectral response, with the CuI device showing slightly higher EQE corresponding to its higher short-circuit current density (CuI  $J_{\text{SC}} = 17.8 \text{ mA}/\text{cm}^2$ , spiro-OMeTAD  $J_{\text{SC}} = 16.1 \text{ mA}/\text{cm}^2$ ). This further highlights the similarity in performance between CuI and spiro-OMeTAD and provides further evidence that there is no reaction between CuI and the  $\text{CH}_3\text{NH}_3\text{PbI}_3$ . Thus, the primary differences in photovoltaic performance of these solar cells are the open-circuit voltage and fill factor.

To determine the relative stability of the CuI and spiro-OMeTAD solar cells, representative solar cells were held at short-circuit conditions under constant 100  $\text{mW}/\text{cm}^2$  AM 1.5G illumination for a period of 2 h in without encapsulation under ambient conditions (Figure 4B). The CuI solar cell showed

**Table 1.** Summary of  $\text{CH}_3\text{NH}_3\text{PbI}_3$  Perovskite Solar Cells Using CuI and Spiro-OMeTAD

hole conductor		$J_{\text{SC}}$ ( $\text{mA}/\text{cm}^2$ )	$V_{\text{OC}}$ (V)	FF	$\eta$ (%)
CuI	champion	17.8	0.55	0.62	6.0
	average <sup>a</sup>	$12.1 \pm 3.3$	$0.52 \pm 0.06$	$0.60 \pm 0.07$	$3.7 \pm 1.1$
	maximum <sup>b</sup>	18.9	0.62	0.71	—
spiro-OMeTAD	champion	16.1	0.79	0.61	7.9
	average <sup>a</sup>	$14.0 \pm 1.7$	$0.78 \pm 0.02$	$0.55 \pm 0.07$	$6.0 \pm 1.1$
	maximum <sup>b</sup>	17.0	0.82	0.65	—

<sup>a</sup>Average parameters were calculated along with a standard deviation from a sample size of 36 CuI and 48 spiro-OMeTAD solar cells (measured area of the electrodes was  $0.13 \pm 0.02 \text{ cm}^2$ ). <sup>b</sup>Parameter maxima are the highest observed value for that parameter in the sample set. See Supporting Information for the complete distribution of solar cell performance.

constant current for the duration of the experiment while the  $J_{SC}$  of the spiro-OMeTAD solar cell decreased by approximately 10%. The stability of the CuI-based perovskite devices is surprising given the poor stability of solid-state dye-sensitized solar cells utilizing CuI.<sup>30</sup> Further investigation is required to elucidate the photostability under long-term illumination. Despite the promising photocurrent stability of CuI, it should be noted that continuous illumination at open-circuit for a period of 1 h causes a decrease ( $\sim 20\%$ ) in  $V_{OC}$  (Figure SI-6A, Supporting Information). This decrease is not due to photodegradation of the CuI or perovskite film as evident from the recovery of original voltage and photovoltaic performance the solar cell upon storage in dark (Figure SI-6B, Supporting Information). Thermal effects and other charge transport issues causing this decrease in photovoltage during illumination are currently being explored. The stability of CuI solar cells at high humidity is also of interest. While no systematic investigation was undertaken in the present work, CuI solar cells were found to be quite stable upon storage without encapsulation under ambient conditions on the benchtop for a period of 54 days, as shown in Figure SI-6C, Supporting Information.

**Impedance Spectroscopy.** Impedance spectroscopy (IS) can be used to separate processes occurring with different characteristic time scales in solar cells, such as the carrier conductivity, recombination resistance, and the chemical capacitance.<sup>31–34</sup> We employed IS to probe the factors responsible for the high fill factor ( $0.60 \pm 0.07$  vs  $0.55 \pm 0.07$ ) and low voltage ( $0.52 \pm 0.06$  V vs  $0.78 \pm 0.02$  V) of CuI compared to spiro-OMeTAD solar cells, as shown in Table 1. Impedance spectra of representative CuI (Figure 5A) and spiro-OMeTAD (Figure 5B) solar cells were recorded at different voltages over the frequency range of 1 Hz to 300 kHz under  $100 \text{ mW/cm}^2$  AM 1.5 illumination. The Nyquist plots of these solar cells show two main features: (i) an arc at high frequencies which becomes almost nonexistent in the case of CuI, and (ii) a second arc at lower frequency.

As in a previous report on  $\text{CH}_3\text{NH}_3\text{PbI}_3$  by Kim et al.,<sup>31</sup> no distinct transmission line (TL) behavior is observed under illumination in the present experiments. The absence of TL behavior, which arises from electron transport resistance, is likely due to the very thin  $\text{TiO}_2$  films employed. Consequently, the low electron transport resistance does not allow for the adequate resolution of any TL feature. Therefore, the simplified circuit model, shown in Figure 5C, represents the case in which no TL is observed. Previously, a similar simplification was made by Boix et al. for  $\text{TiO}_2/\text{Sb}_2\text{S}_3/\text{CuSCN}$  solar cells which did not exhibit a marked TL component.<sup>33</sup> In this equivalent circuit model, the high frequency arc in the Nyquist plots is attributed to the diffusion of holes through the hole transport material (HTM) which is modeled by a HTM resistance,  $R_{HTM}$ , in parallel with HTM capacitance,  $C_{HTM}$ . The lower frequency arc is attributed to a recombination resistance,  $R_{rec}$ , in parallel with a chemical capacitance,  $c_\mu$ , related to the electron Fermi level in the  $\text{TiO}_2$ .

Recombination in CuI and spiro-OMeTAD solar cells was investigated by the change in recombination resistance (inversely related to the recombination rate) with voltage as shown in Figure 6A. Recombination resistance,  $R_{rec}$ , decreases exponentially for both CuI and spiro-OMeTAD with increasing potential, a behavior typical of mesoporous  $\text{TiO}_2$  solar cells.<sup>32,33</sup> At low potentials, recombination in both systems becomes dominated by shunting, resulting in a flattening of the slope of

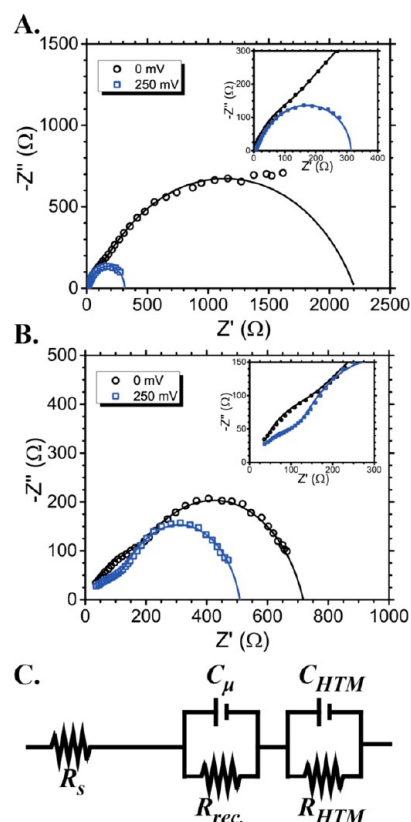


**Figure 5.** Representative Nyquist plots at short-circuit and 250 mV bias of  $\text{TiO}_2/\text{CH}_3\text{NH}_3\text{PbI}_3$  solar cells under  $100 \text{ mW/cm}^2$  illumination employing (A) CuI and (B) spiro-OMeTAD hole conductors. Insets show the high frequency portion of the spectra. (C) Equivalent circuit model employed for impedance analysis of the perovskite solar cells.

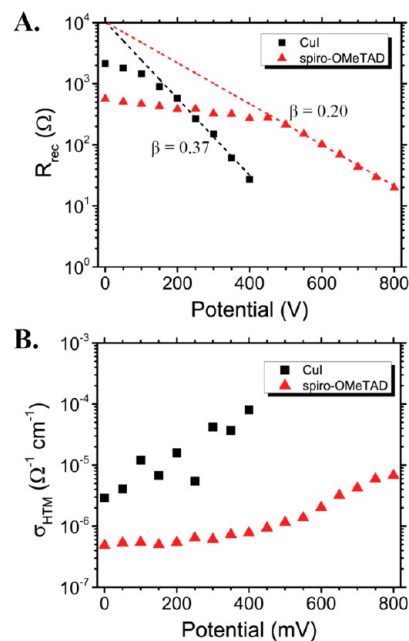


**Figure 6.** (A) Summary of the recombination resistance,  $R_{rec}$ . Dashed line shows the fit of the linear portion at high potentials to eq 2. (B) Hole transport material conductivity,  $\sigma_{HTM}$ , of CuI and spiro-OMeTAD solar cells at different potentials under  $100 \text{ mW/cm}^2$  AM 1.5 illumination.



$R_{\text{rec}}^{33}$  In spiro-OMeTAD, shunting appears to dominate recombination up to 500 mV, while with CuI, shunting only appears at very low potential (<200 mV). This indicates that recombination in the mesoscale superstructure of the  $\text{TiO}_2/\text{CH}_3\text{NH}_3\text{PbI}_3/\text{spiro-OMeTAD}$  device is low compared to CuI-based devices, so it does not become the dominant recombination pathway until high potential (>500 mV) is reached. Thus, it is seen that CuI displays much higher recombination, seen by lower  $R_{\text{rec}}$  at comparable potentials, which limits the open-circuit voltage of these devices.

On the other hand, the slope of  $R_{\text{rec}}$  near the respective open-circuit voltage is greater for CuI than spiro-OMeTAD. Assuming the diode model of solar cell performance, recombination can be described by eq 1.

$$U_n = k_{\text{rec}} n_c^\beta \quad (1)$$

where  $U_n$  is the recombination rate,  $k_{\text{rec}}$  is the recombination rate constant,  $n_c$  is the population of free electrons, and  $\beta$  is the recombination exponent (where  $0 \leq \beta \leq 1$ ) which is related to the diode quality factor,  $m$ , by  $m = 1/\beta$ .<sup>32</sup> From this model, the recombination resistance can be calculated by eq 2.<sup>32</sup>

$$R_{\text{rec}} = \frac{k_B T}{q \beta j_0} e^{-q \beta V_F / k_B T} \quad (2)$$

where  $j_0$  is the diode dark current, and  $V_F$  is the difference in electrode Fermi level potential. Therefore, the difference in the slope of  $R_{\text{rec}}$  is attributed to a lower diode ideality factor for CuI than spiro-OMeTAD ( $m_{\text{CuI}} = 2.7$ ,  $m_{\text{spiro}} = 5.0$ ). This lower diode quality factor (closer to ideal) explains the increased fill factor seen in CuI solar cells.

The conductivity of the HTM,  $\sigma_{\text{HTM}}$  (Figure 6B), was estimated from  $R_{\text{HTM}}$  as  $\sigma_{\text{HTM}} = L/R_{\text{HTM}}$  where  $L$  is the length traveled by holes which is the sum of the HTM overlayer thickness as measured by SEM and the thickness of the  $\text{TiO}_2$  layer divided by 2 to account for the travel of holes inside the  $\text{TiO}_2$  network.<sup>33</sup> From this, it is seen that the conductivity of CuI is nearly 2 orders of magnitude higher than that of spiro-OMeTAD. The higher electrical conductivity of CuI, which is consistent with previously published results,<sup>19,22,29</sup> leads to a lower resistive voltage loss due to hole transport. Therefore, the higher diode quality factor (and fill factor) of CuI can be explained by an electrical conductivity greater than that of spiro-OMeTAD.

The primary reason for the low efficiency of the CuI solar cells compared to the best spiro-OMeTAD solar cells was the low open-circuit voltage obtained using CuI. This low  $V_{\text{OC}}$  is attributed to a recombination rate with CuI higher than that of spiro-OMeTAD. It was previously reported in solid-state DSCs that free iodine in CuI can induce valence band trap states which decrease  $V_{\text{OC}}$  and increase recombination.<sup>16</sup> Further evidence is needed to determine if this is occurring in these devices, but, if it is the cause of the low  $V_{\text{OC}}$ , proper passivation of these trap states could lead to higher  $V_{\text{OC}}$  and better overall photovoltaic performance.

## CONCLUSIONS

We have demonstrated CuI as a solution-processable, inorganic hole conductor for use in methylammonium lead iodide perovskite solar cells. These solar cells show power conversion efficiencies as high as 6.0% and are shown to be very stable, providing a  $J_{\text{SC}}$  stability better than that of spiro-OMeTAD solar cells upon continuous 2 h illumination. In addition, CuI

provides fill factors higher than that of spiro-OMeTAD because of higher electrical conductivity. However, despite these advantages, the efficiency obtained with CuI is still lower than with spiro-OMeTAD because of the exceptionally high voltages obtained in spiro-OMeTAD solar cells. Future studies are aimed toward determining whether the high recombination seen in CuI-based solar cells can be reduced and higher  $V_{\text{OC}}$  obtained. Despite these potential difficulties, CuI represents a promising low-cost hole conductor for perovskite solar cells. In fact, a CuI solar cell exhibiting the performance of the maximum parameter values from Table 1 ( $J_{\text{SC}} = 18.9 \text{ mA/cm}^2$ ,  $V_{\text{OC}} = 0.62 \text{ V}$ , and  $\text{FF} = 0.71$ ) would yield an efficiency of 8.3%, making CuI a promising inorganic hole conductor material for use with organo-lead halide perovskite.

## ASSOCIATED CONTENT

### Supporting Information

$J$ - $V$  curves of masked and scribed CuI solar cells, UV-visible absorption spectra, a summary of the performance of all CuI and spiro-OMeTAD devices and a comparison to other published results, and  $V_{\text{OC}}$  with extended illumination. This material is available free of charge via the Internet at <http://pubs.acs.org>.

## AUTHOR INFORMATION

### Corresponding Author

[pkamat@nd.edu](mailto:pkamat@nd.edu)

### Present Address

<sup>#</sup>University of Waterloo, Canada.

### Notes

The authors declare no competing financial interest.

## ACKNOWLEDGMENTS

The research described herein was supported by the Division of Chemical Sciences, Geosciences, and Biosciences, Office of Basic Energy Sciences of the U.S. Department of Energy, through award DE-FC02-04ER15533. This is contribution number NDRL No. 4987 from the Notre Dame Radiation Laboratory.

## REFERENCES

- (1) Kamat, P. V. *J. Phys. Chem. C* **2007**, *111*, 2834–2860.
- (2) Kamat, P. V. *J. Phys. Chem. C* **2008**, *112*, 18737–18753.
- (3) Park, N. *J. Phys. Chem. Lett.* **2013**, *4*, 2423–2429.
- (4) Kamat, P. V. *J. Phys. Chem. Lett.* **2013**, *4*, 908–918.
- (5) Mora-Seró, I.; Bisquert, J. *J. Phys. Chem. Lett.* **2010**, *1*, 3046–3052.
- (6) Hodes, G. *Science* **2013**, *342*, 317–318.
- (7) Dale, M.; Benson, S. M. *Environ. Sci. Technol.* **2013**, *47*, 3482–3489.
- (8) Burschka, J.; Pellet, N.; Moon, S.-J.; Humphry-Baker, R.; Gao, P.; Nazeeruddin, M. K.; Grätzel, M. *Nature* **2013**, *499*, 316–319.
- (9) Heo, J. H.; Im, S. H.; Noh, J. H.; Mandal, T. N.; Lim, C.; Chang, J. A.; Lee, Y. H.; Kim, H.; Sarkar, A.; Nazeeruddin, M. K.; Grätzel, M.; Seok, S. I. *Nat. Photonics* **2013**, *7*, 486–491.
- (10) Noh, J. H.; Im, S. H.; Heo, J. H.; Mandal, T. N.; Seok, S. I. *Nano Lett.* **2013**, *13*, 1764–1769.
- (11) Snaith, H. J. *J. Phys. Chem. Lett.* **2013**, *4*, 3623–3630.
- (12) Abrusci, A.; Stranks, S. D.; Docampo, P.; Yip, H.-L.; Jen, A. K.-Y.; Snaith, H. J. *Nano Lett.* **2013**, *13*, 3124–3128.
- (13) Edri, E.; Kirmayer, S.; Cahen, D.; Hodes, G. *J. Phys. Chem. Lett.* **2013**, *4*, 897–902.
- (14) Liu, M.; Johnston, M. B.; Snaith, H. J. *Nature* **2013**, *501*, 395–398.

- (15) Kim, H.-S.; Lee, C.-R.; Im, J.-H.; Lee, K.-B.; Moehl, T.; Marchioro, A.; Moon, S.-J.; Humphry-Baker, R.; Yum, J.-H.; Moser, J. E.; Grätzel, M.; Park, N.-G. *Sci. Rep.* **2012**, *2*, 591.
- (16) Perera, V. P. S.; Tennakone, K. *Sol. Energy Mater. Sol. Cells* **2003**, *79*, 249–255.
- (17) Zhang, K.; Wang, L.; Liang, Y.; Yang, S.; Liang, J.; Cheng, F.; Chen, J. *Synth. Met.* **2012**, *162*, 490–496.
- (18) Li, B.; Wang, L.; Kang, B.; Wang, P.; Qiu, Y. *Sol. Energy Mater. Sol. Cells* **2006**, *90*, 549–573.
- (19) Rusop, M.; Soga, T.; Jimbo, T.; Umeno, M. *Surf. Rev. Lett.* **2004**, *11*, 577–583.
- (20) O'Regan, B.; Lenzmann, F.; Muis, R.; Wienke, J. *Chem. Mater.* **2002**, *14*, 5023–5029.
- (21) Christians, J. A.; Kamat, P. V. *ACS Nano* **2013**, *7*, 7967–7974.
- (22) Wagner, J. B.; Wagner, C. J. *Chem. Phys.* **1957**, *26*, 1597–1601.
- (23) Tennakone, K.; Kumara, G. R. R. a; Kumarasinghe, a R.; Wijayantha, K. G. U.; Sirimanne, P. M. *Semicond. Sci. Technol.* **1995**, *10*, 1689–1693.
- (24) Moon, S.-J.; Itzhaik, Y.; Yum, J.-H.; Zakeeruddin, S. M.; Hodes, G.; Grätzel, M. J. *Phys. Chem. Lett.* **2010**, *1*, 1524–1527.
- (25) Chang, J. A.; Im, S. H.; Lee, Y. H.; Kim, H.-J.; Lim, C.-S.; Heo, J. H.; Seok, S. I. *Nano Lett.* **2012**, *12*, 1863–1867.
- (26) Nezu, S.; Larramona, G.; Choné, C.; Jacob, A.; Delatouche, B.; Péré, D.; Moisan, C. J. *Phys. Chem. C* **2010**, *114*, 6854–6859.
- (27) Kavan, L.; Grätzel, M. *Electrochim. Acta* **1995**, *40*, 643–652.
- (28) O'Regan, B. C.; Lenzmann, F. J. *Phys. Chem. B* **2004**, *108*, 4342–4350.
- (29) Lee, M. M.; Teuscher, J.; Miyasaka, T.; Murakami, T. N.; Snaith, H. J. *Science* **2012**, *338*, 643–647.
- (30) Tennakone, K.; Kumara, G. R. R. A.; Kumarasinghe, A. R.; Wijayantha, K. G. U.; Sirimanne, P. M. *Semicond. Sci. Technol.* **1995**, *10*, 1689–1693.
- (31) Kim, H.-S.; Mora-Sero, I.; Gonzalez-Pedro, V.; Fabregat-Santiago, F.; Juarez-Perez, E. J.; Park, N.-G.; Bisquert, J. *Nat. Commun.* **2013**, *4*, 2242.
- (32) Fabregat-Santiago, F.; Garcia-Belmonte, G.; Mora-Seró, I.; Bisquert, J. *Phys. Chem. Chem. Phys.* **2011**, *13*, 9083–9118.
- (33) Boix, P. P.; Larramona, G.; Jacob, A.; Delatouche, B.; Mora-Seró, I.; Bisquert, J. *J. Phys. Chem. C* **2012**, *116*, 1579–1587.
- (34) Boix, P. P.; Lee, Y. H.; Fabregat-Santiago, F.; Im, S. H.; Mora-Sero, I.; Bisquert, J.; Seok, S. I. *ACS Nano* **2012**, *6*, 873–880.